Inorganic Chemistry

Article

pubs.acs.org/IC

Role of the Sintering Temperature and Doping Level in the Structural and Spectral Properties of Eu-Doped Nanocrystalline YVO_4

R. J. Wiglusz,* A. Bednarkiewicz, and W. Strek

Institute of Low Temperature and Structure Research, Polish Academy of Sciences, P.O. Box 1410, 50-950 Wroclaw 2, Poland

ABSTRACT: A sol−gel approach was employed to prepare nanosized YVO_4 nanopowders doped with Eu^{3+} ions. Raw nanomaterials were thermally treated at 700−1000 °C for 3 h. X-ray diffraction (XRD) analysis demonstrated that single-phase nanopowders with high crystallite dispersion were obtained. Our studies were focused on relating the luminescence properties of the Eu^{3+} dopant to the nanocrystallite (NC) size. Depending on the thermal treatment, the average NC size was calculated to range from 20 nm to 1.1 μm. We have found that the size effect manifests mainly in the expansion of the cell volume and broadening of XRD peaks, as indicated by Rietveld analysis. Moreover, emission and excitation spectra, although typical for the Eu^{3+} ions, demonstrated some degree of correlation with the calcination temperature and doping concentration. To explain these differences a detailed analysis of the luminescence spectra by the Judd−Ofelt theory has been performed.

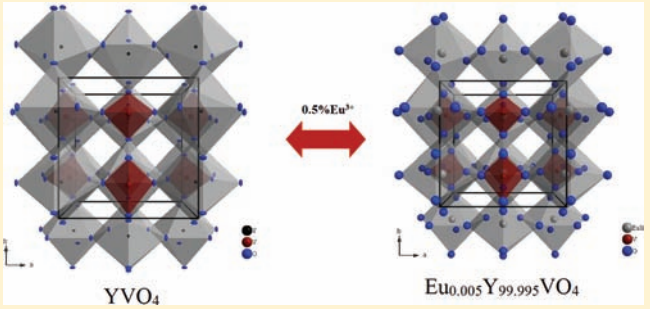

INTRODUCTION

Yttrium orthovanadate (YVO_4) has been broadly used as a laser host material[1,2] because of its outstanding thermal, mechanical, and optical properties. This matrix has also been employed to produce phosphors that can emit various colors from f−f transitions.[3] Many synthesis routes have been developed to prepare these YVO_4 hosts doped with rare-earth ions. A high-temperature solid-state reaction is a conventional method, which is simple but has several disadvantages, such as high energy consumption and agglomeration of particles.[4,5] Wet-chemistry methods have been proposed as well and proved to be the most powerful technique for preparing single-phase and well-crystalline YVO_4. Representative examples include the sol−gel process,[6,7] solution combustion synthesis,[8] coprecipitation reaction,[9] and low-temperature hydrothermal methods.[10−12] Among the enumerated methods, hydrothermal synthesis is one of the most promising because it allows one to obtain particles with high crystallinity, narrow size distribution, and high purity at mild reaction conditions without milling or further calcination treatment.[13] Furthermore, the hydrothermal method can easily control the size and morphology of the crystals through the regulations of the starting material quantity, reaction temperature, and time. Wu et al.[14] reported the synthesis of either well-defined YVO_4 microcrystals with clear facets in strongly acidic media or nanoflakes with dimensions of 5−50 nm in basic media. Wang et al.[15] prepared a single phase of Eu^{3+}-doped YVO_4 nanophosphors at different pH values (pH = 7−11) by a mild hydrothermal method. Wu et al.[16] synthesized YVO_4 nanorods/microtubes by the hydrothermal reaction of $(NH_4)_{0.5}V_2O_5$ nanowire templates with Y^{3+}. This group has also synthesized rod-, olive-, and pineapple-shaped nanocrystals of YVO_4:Eu^{3+} using porous silicon substrates, mixed with V_2O_5 nanowires, and cetyl trimethylammonium bromide (CTAB) additives.[17] Wang et al.[18] prepared nano- and microscaled Eu-doped yttrium orthovanadate powders via a hydrothermal method in a wide pH range controlled by disodium ethylenediaminetetraacetic acid assisted morphology.

In this article, we study the impact of the Eu^{3+} dopant concentration and sintering temperature on their structural and optical property characterization of the yttrium orthovanadates. Among all of the lanthanides, Eu^{3+} is most convenient for these kinds of studies because of the relatively narrow band emission and long lifetimes of the excited states. More importantly, Eu^{3+} doping is regarded as a luminescent probe that allows extraction of the necessary information concerning the local chemical environment of lanthanide and structure directly from the emission spectra. Splitting of the $^5D_0 \rightarrow {}^7F_0$ Eu^{3+} electron transition was used in order to determine the symmetry of the position occupied by the doping ion within the crystal structure of the host matrix. The Judd−Ofelt theory was applied to calculate the radiative properties of the prepared materials, and the variability of the asymmetry ratio between $^5D_0 \rightarrow {}^7F_2$ and $^5D_0 \rightarrow {}^7F_1$ electron transitions was studied.

EXPERIMENTAL SECTION

Synthesis. Nanocrystalline tetragonal YVO_4 doped with Eu^{3+} ions was prepared by the sol−gel process. The concentration of the optically active Eu^{3+} ions has been set to 0.5, 1, 2, and 5 mol % with respect to the appropriate Y^{3+} molar content. Analytical-grade Y_2O_3, Eu_2O_3, and V_2O_5 oxides were used as the starting materials. In this method, stoichiometric amounts of Y_2O_3 and Eu_2O_3 were digested in excess of diluted HNO_3 in order to transform them into nitrate salts. V_2O_5 was processed in excess of diluted NH_4OH in order to transform

Received: November 14, 2011
Published: December 23, 2011

   dx.doi.org/10.1021/ic202444s | *Inorg. Chem.* 2012, 51, 1180−1186

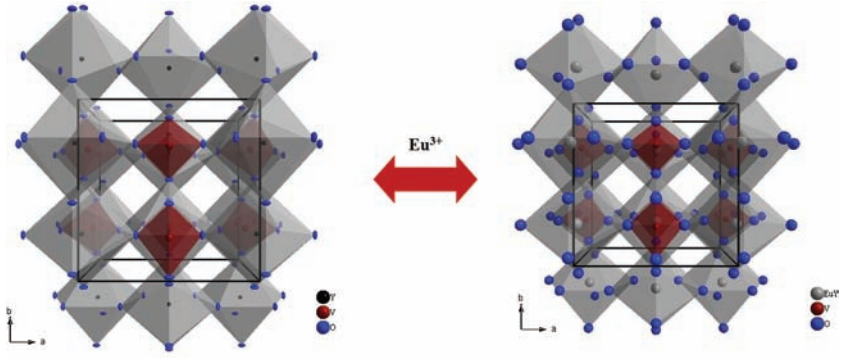

Figure 1. Projection of the YVO_4 structure along the *b* axis [20] and the 0.5% Eu:YVO_4 structure along the *b* axis.

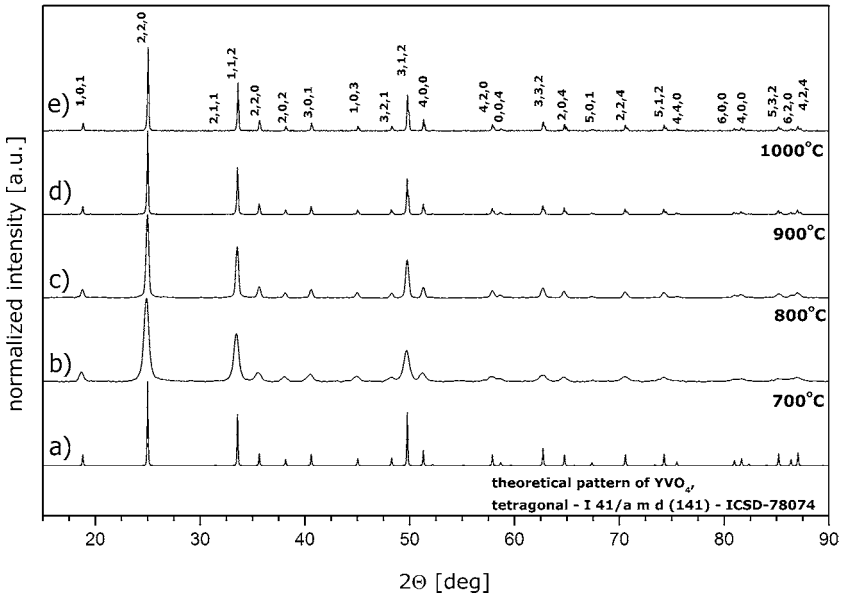

Figure 2. Theoretical [a; tetragonal *I*41/*amd* (No. 141), ICSD-78074] and representative XRD patterns for 1% Eu-doped YVO_4 nanopowders annealed at (b) 700, (c) 800, (d) 900, and (e) 1000 °C.

it into an ammonium salt, which was mixed with the obtained nitrates. In the next step, citric acid and poly(ethylene glycol) were added, and then the obtained solution was heated to 80 °C to make it viscous. In that way, the obtained resin containing proper molar ratios of all substrates was annealed at the temperature range 700−1000 °C every 100 °C for 3 h, and then the white-yellow powder of YVO_4 doped with Eu^{3+} ions was formed. The former reaction could be written as follows:

$$NH_4VO_3 + (1 - x)Y(NO_3)_3 + xEu(NO_3)_3 \xrightarrow{H_2O:T} Eu_x{:}\ Y_{1-x}VO_4 + NH_4^+ + 9NO_3^- \quad (1)$$

where $x = 0.005-0.05$.

X-ray Diffraction (XRD) and Transmission Electron Microscopy (TEM) Analysis. In order to check the development of the crystal phase, XRD patterns of the prepared materials were obtained after heating at 700−1000 °C for 3 h. The XRD patterns were collected in the 2θ range of 5−120° with an X'Pert PRO X-ray diffractometer (Cu $K\alpha_1$, 1.540 60 Å; PANalytical). The XRD patterns were assigned using the Joint Committee on Powder Diffraction Standards database and then were analyzed. Scherrer's relation, eq 2, was used to estimate the sizes of the obtained crystallites.[19]

$$D = \frac{0.9\lambda}{\cos\theta\sqrt{\beta^2 - {\beta_0}^2}} \quad (2)$$

In this equation, D is the average crystallite size, λ denotes the X-ray radiation wavelength, β represents a full width at half-maximum of a diffraction line located at θ, and β_0 represents a scan aperture of the diffractometer. The Eu:YVO_4 nanoparticles were investigated by a high-resolution TEM (HRTEM) using a Philips CM-20 Super Twin microscope, operating at 200 kV. Samples for HRTEM were prepared by dispersing a powder in methanol and leaving a droplet of the suspension on a copper microscope grid covered with perforated carbon.

Emission and Excitation Spectra. Emission spectra were measured with a Jobin-Yvon THR1000 spectrophotometer equipped with a CCD detector and a 1200 L/mm holographic grating blazed at 500 nm. As the excitation source, pulsed (10 Hz) fourth harmonics (266 nm) of a Nd:YAG laser was used. The detection setup exhibits a relatively flat response in the spectral range of interest. Excitation spectra ($\lambda_{monitoring}$ = 620 nm) were measured with a FluoroMax-3/Horiba Jobin-Yvon/2007 instrument. Excitation spectra have been corrected for the excitation light intensity.

Emission lifetimes were measured at 616 nm (under 266 nm excitation, fourth harmonics of a Nd:YAG laser, LOTIS TII with Harmonic Generators for Nd:YAG lasers HG-TF, Belarus) using a Jobin-Yvon THR 1000 spectrophotometer, a Hamamatsu R928 photomultiplier as a detector, and a digital LeCroy WaveSurfer oscilloscope for data collection. The decay curve fitting was performed with single decay model in *Origin* 7.5 software. The luminescence lifetime decays $I(t)$ were analyzed either as an averaged luminescence lifetime $\langle\tau\rangle$ calculated as $\langle t\rangle \int I(t)\ t\ dt / \int I(t)\ dt$, which was used for for Judd−Ofelt analysis, or with double-exponential function $y(t) = B + A_1$

dx.doi.org/10.1021/ic202444s | *Inorg. Chem.* 2012, 51, 1180−1186

Table 1. Unit Cell Parameters (a and c), Relative Cell Volume Variation [$(x - x_{SC})/x_{SC}$, $x = a, c$], Single-Crystal Cell Volume (V), Theoretical Grain Size Calculated According to the Sherrer (S) amd Rietveld (R) Methods, as Well as Refined Factors (R_w) Presented for Eu^{3+}-Doped YVO_4 Nanoparticles as a Function of the Dopant Concentration and Sintering Temperature

Eu [%]	annealing temp [°C]	a [Å]	$(a - a_{SC})/a_{SC}$ [%]	c [Å]	$(c - c_{SC})/c_{SC}$ [%]	V [Å^3]	S [nm]	R [nm]	R_w [%]
	single crystal [20]	7.1180		6.2893		318.681(4)			
0.5	700	7.1202	0.031	6.2947	0.086	319,124(0)	32	26	3.2
	800	7.1218	0.053	6.2936	0.068	319,211(6)	512	304	4.4
	900	7.1228	0.067	6.2946	0.084	319,352(0)	2280	1712	5.0
	1000	7.1240	0.084	6.2950	0.091	319,480(0)	1185	671	5.2
1.0	700	7.1157	−0.032	6.2921	0.045	318,589(1)	21	15	4.5
	800	7.1268	0.124	6.3027	0.213	320,122(2)	64	54	5.9
	900	7.1236	0.079	6.2950	0.091	319,444(0)	416	353	4.3
	1000	7.1243	0.089	6.2955	0.099	319,532(2)	592	339	4.5
2.0	700	7.1205	0.035	6.2961	0.108	319,221(8)	35	28	3.5
	800	7.1237	0.080	6.2980	0.138	319,605(2)	108	71	3.8
	900	7.1241	0.086	6.2943	0.080	319,453(3)	243	102	4.3
	1000	7.1244	0.090	6.2955	0.099	319,541(2)	1027	667	4.5
5.0	700	7.1248	0.096	6.2938	0.072	319,490(7)	27	18	4.2
	800	7.1273	0.131	6.3000	0.170	320,030(0)	33	23	4.3
	900	7.1271	0.128	6.3010	0.186	320,062(8)	40	32	3.4
	1000	7.1282	0.143	6.3015	0.194	320,207(3)	72	49	4.2

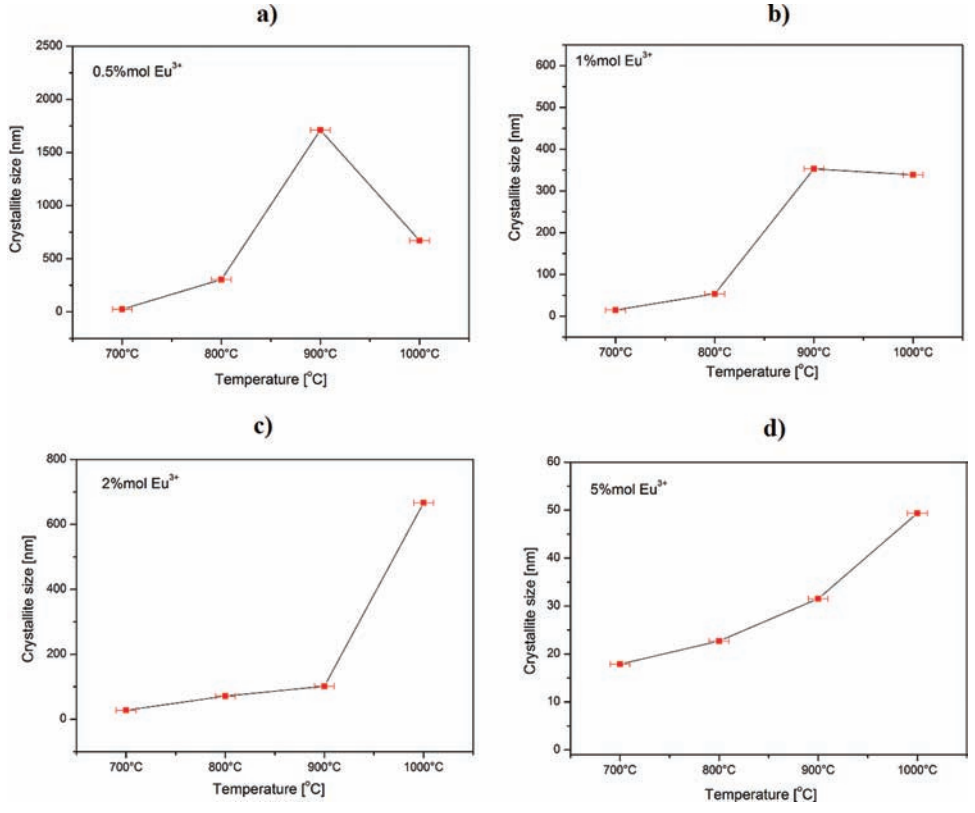

Figure 3. Average grain size of the crystallites as a function of the temperature [°C] calculated by Rietveld analysis.

$\exp(-t/\tau_1) + A_2 \exp(-t/\tau_1)$, where A_1, A_2, t_1, and t_2 correspond to short (index 1) and long (index 2) amplitudes (A) and luminescence decay (τ).

RESULTS AND DISCUSSION

Structural Analysis. The yttrium vanadate YVO_4 has a zircon structure [space group $I4_1/amd$ (No. 141) and lattice parameters a = 7.1183 Å and c = 6.2893 Å][20] with lanthanide ion dopants substituting yttrium ions in D_{2d} site symmetry (see Figure 1). The formation of the crystalline YVO_4 doped with 0.5−5 mol % of Eu^{3+} powders was studied by XRD measurements (see Figure 2). The crystal phase could be detected for all doping concentrations already at 700 °C and at least up to 1000 °C. The comparison of the resulting XRD patterns with the reference standard of YVO_4 (ICSD-78074) confirmed the presence of a pure orthovanadate structure without any structural impurities.

The cell parameters were calculated with the help of Rietveld analysis[21] using an anisotropic approach[22] and *Maud 2.0* software.[23] On the basis of the results presented in Table 1, a general trend

dx.doi.org/10.1021/ic202444s | *Inorg. Chem.* 2012, 51, 1180−1186

could be found. All of the unit cell parameters decrease with an increase in the annealing temperature or, in other words, with an increase of the grain size (see Figure 3). The unit cell parameters for nanoparticles were found to be significantly larger in comparison to the YVO_4 single crystal. Reduction of the particle size and the resulting negative pressure on the crystal lattice lead directly to lattice cell volume expansion.[24,25]

According to the TEM study (Figure 4a), the particles of 0.5% Eu:YVO_4 sintered at 700 °C are elongated, reminding one

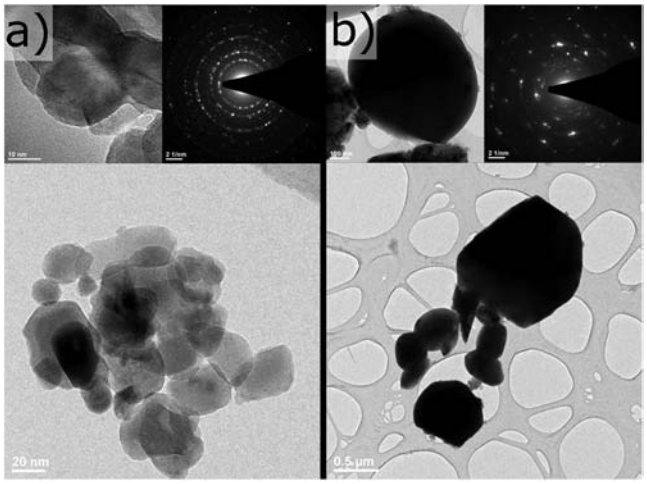

Figure 4. SAED and TEM images of selected YVO_4 materials doped with 0.5 mol % Eu ion annealed at (a) 700 and (b) 1000 °C.

of the shape of flat plates and forming large groups of agglomerates with an average size of 20 nm. However, the TEM images (Figure 4b) of 0.5% Eu:YVO_4 sintered at 1000 °C are rounded with an average size of 500 nm. Analysis of the selected-area electron diffraction (SAED) images (insets of Figure 4a,b) reveals the presence of very sharp, individual spots from crystalline particles at positions corresponding to the tetragonal phase of YVO_4.

Luminescent Properties. *Excitation Spectra.* Figure 5 shows the representative excitation spectra of 1000 °C YVO_4-doped

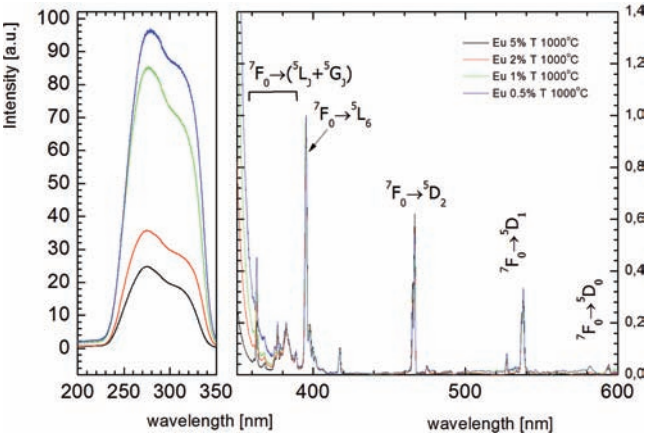

Figure 5. Excitation spectra of 1000 °C sintered sample for different Eu^{3+} concentration. Transitions $^8S_{7/2} \rightarrow ^6D_J$, ^6I_J, ^6P_J are hidden behind much stronger Eu−O charge transfer band (CT).

Eu^{3+} ions in a concentration series monitored at λ_{em} = 619 nm. The two strong and broad excitation bands at around 240−350 nm were observed. The broad band at about 320 nm was assigned to the charge-transfer (CT) band of $Eu^{3+}-O^{2-}$ resulting from an electron transfer from the ligand $O^{2-}(2p^6)$ orbitals to the empty states of $4f^6$ for the Eu^{3+} configuration. The band at about 260 nm was assigned to absorption of the host lattice.[26] Around 100 times weaker and narrow f−f electronic lines within $4f^6$ for the Eu^{3+} configuration can also be observed. The transitions $^7F_0 \rightarrow ^5L_J + ^5G_J$, $^7F_0 \rightarrow ^5D_2$, and $^7F_0 \rightarrow ^5D_1$ can be observed at 370−410, 466, and 52−540 nm, respectively. While the f−f transitions are not susceptible to the Eu^{3+} concentration, the CT band peak position and intensity change with the Eu^{3+} content and sintering temperature, as presented in Figure 6. The changes are not very strong, which implies that

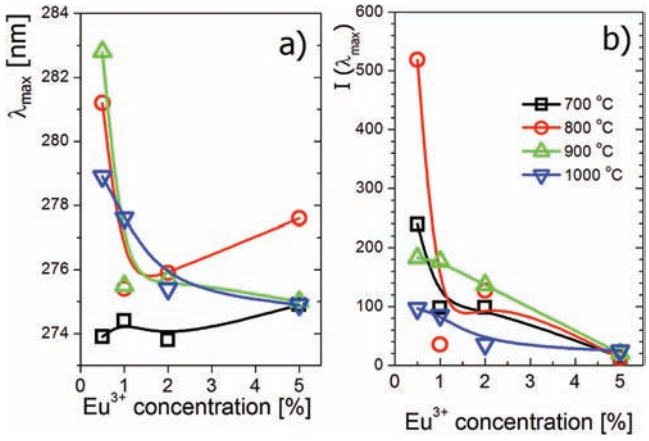

Figure 6. Position (λ_{max}) (a) and relative intensity [$I(\lambda_{max})$] (b) of the CT band with respect to the $^7F_0 \rightarrow ^5L_J + ^5G_J$ transitions as a function of the dopant concentration.

the energy gap between the ground and excited states of the vanadate group is not affected for Eu^{3+} above 1% and is only slightly different for 800 °C sintered low 0.5% doped samples.

There are a few other factors contributing to variation of the position and intensity of the CT band. Xie et al.[27] observed a monotonic red shift of the CT peak position wavelength with an increase of the YVO_4:Eu^{3+} nanoparticle concentration in a colloidal solution. Simultaneously, the intensity of the CT band sharply increased for low Eu^{3+} doping and decreased gradually with a Eu^{3+} concentration larger than 2.5 mM. This observation was explained by significant luminescence quenching and further suggests that the YVO_4 nanoparticle within the solution interact with each other. Moreover, efficient electron transfer between vanadate groups has been previously observed over an average migration distance of ~9 nm.[28] In the course of energy migration, some of the energy may be lost/gained because of phonon-assisted energy transfer, and the resulting red or blue shift of the CT band may be observed, respectively.

Therefore, for a low 0.5% Eu^{3+} sample, the apparent red shift (see Figure 6a) can be correlated with the increase of the CT band intensity (see Figure 6c) for increasing sintering temperature. This may indicate a vanishing amorphous phase, the formation of a crystalline structure, and phonon accessibility when the sintering temperature was raised from 700 °C and up. Currently, we cannot explain the blue shift and CT intensity fading observed above 900 °C. The blue shift (see Figure 6b) and decrease of the CT intensity (see Figure 6d) may be correlated with increasing Eu^{3+} concentration. The Eu^{3+} ions most

dx.doi.org/10.1021/ic202444s | *Inorg. Chem.* 2012, 51, 1180−1186

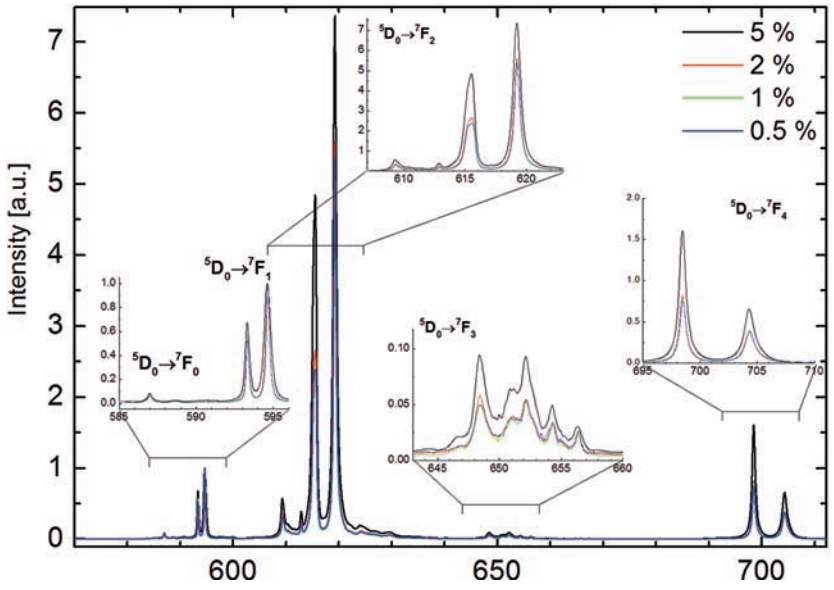

Figure 7. Example luminescence spectra of $^5D_0$ Eu^{3+} of YVO_4 sintered at 1000 °C doped with variable amounts of Eu^{3+} ions.

probably compete with vanadate groups during energy migration within or between the nanocrystal.

Emission Spectra. The emission spectra were measured at room and liquid-nitrogen temperatures at a recorded emission wavelength of 619.2 nm corresponding to the $^5D_1 \rightarrow ^7F_2$ electron transition (see Figure 7); besides typical transitions from the $^5D_0$ level, very weak (ca. 1−5% of the $^5D_0 \rightarrow ^7F_1$ transition intensity) transitions from the $^5D_1$ level can be additionally observed (not shown). The $^5D_1 \rightarrow ^7F_1$ and $^7F_2$ transitions can be found at 538 and 555 nm. The spectra are normalized to the $^5D_0 \rightarrow ^7F_1$ transition, which allows one to notice the relative changes of $^5D_0 \rightarrow ^7F_J$ (J = 1−4) transitions with different doping levels at the same 1000 °C sintering temperature.

Besides highest doping, the emission from the $^5D_0$ level exhibits only relatively insignificant changes of the intensity with the doping level (Figure 7). These may be observed for all of the transitions as well as for the forbidden $^5D_0 \rightarrow ^7F_0$ transition. Moreover, the relative changes of the intensities between the $^5D_0 \rightarrow ^7F_1$ and $^5D_0 \rightarrow ^7F_2$ transitions in the samples sintered in 1000 °C in comparison to 700 °C may be observed. This behavior was studied and quantified with Judd−Ofelt theory.

The hypersensitive $^5D_0 \rightarrow ^7F_2$ emission is the most intensive one in the whole spectrum (see Figure 7). It is around 13.5, 24, and over 5 times more intense (in integral intensity terms) than the $^5D_0 \rightarrow ^7F_1$ (at ∼595 nm), $^5D_0 \rightarrow ^7F_3$ (at ∼652 nm), and $^5D_0 \rightarrow ^7F_4$ (at ∼700 nm) transitions, respectively. The $^5D_0 \rightarrow ^7F_0$ transition at 587 nm has an integral intensity almost 86 times smaller (∼1.1%) than that of the $^5D_0 \rightarrow ^7F_2$ transition. The presence of the $^5D_0 \rightarrow ^7F_0$ transition means the Eu^{3+} ions occupy noncentrosymmetric sites because it is forbidden in the D_{2d} symmetry. Besides a single and well-developed $^5D_0 \rightarrow ^7F_0$ line, three additional weaker lines exist in the spectra at 585, 589, and 591 nm, which potentially may indicate three additional low-population local Eu^{3+} sites.

In the tetragonal D_{2d} symmetry, the ^7F_J manifolds split into two, four, five, and seven Stark components for J = 1−4.[29] The correct number of Stark levels may be found for J = 1−3, but for the $^7F_4$ multiplet, only two instead of seven emission lines may be found in the spectra. It is noticeable that the emission lines are very narrow (i.e., 8.8/13.1, 20.8/18.1, and 14.8/22.4 cm^{-1} for the strongest lines within $^5D_0 \rightarrow ^7F_1$, $^7F_2$, and $^7F_4$ located at 16812.6/16849.7, 16245.4/15144.9, and 14313.0/14194.0 cm^{-1}). The corresponding peaks within doublets are separated by 37.0, 100.5, and 118.9 cm^{-1}, which is in excellent agreement with the literature. The $^5D_0 \rightarrow ^7F_J$ transitions are therefore dominated by the emission to 1′, 2′ ($^7F_1$), 1′, 3′ ($^7F_2$), and 3′, 6′ ($^7F_4$) Stark levels of the respective manifolds.

The fluorescence intensity ratio of $^5D_0 \rightarrow ^7F_2$ to $^5D_0 \rightarrow ^7F_1$ called the asymmetry ratio (AR) is proportional to the degree of asymmetry in the vicinity of Eu^{3+} ions and Eu−O covalency, which is affected by the site symmetry, electronegativity, and covalency of the ligand atoms. Because of thermal treatment, the nanoparticle size increases, leading to the narrowing of Eu^{3+} emission (Figure 8).[28,30] The AR should also decrease, denoting

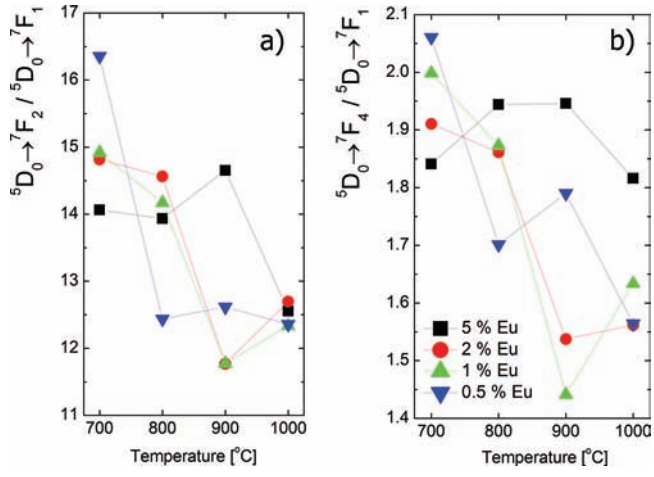

Figure 8. Changes of the relative AR $I(^5D_0 \rightarrow ^7F_2)/I(^5D_0 \rightarrow ^7F_1)$ and $I(^5D_0 \rightarrow ^7F_4)/I(^5D_0 \rightarrow ^7F_1)$ intensities versus sintering temperature.

an increase of the local symmetry at the Eu^{3+} site, resulting from higher crystallinity of the annealed nanocrystal. This is nicely observed for the 700 °C annealed sample, whereas for higher annealing temperatures, the trend is opposite. We found that the grain size increase together with larger doping levels induce deformations to the unit cell, and as a consequence, the local symmetry

dx.doi.org/10.1021/ic202444s | Inorg. Chem. 2012, 51, 1180−1186

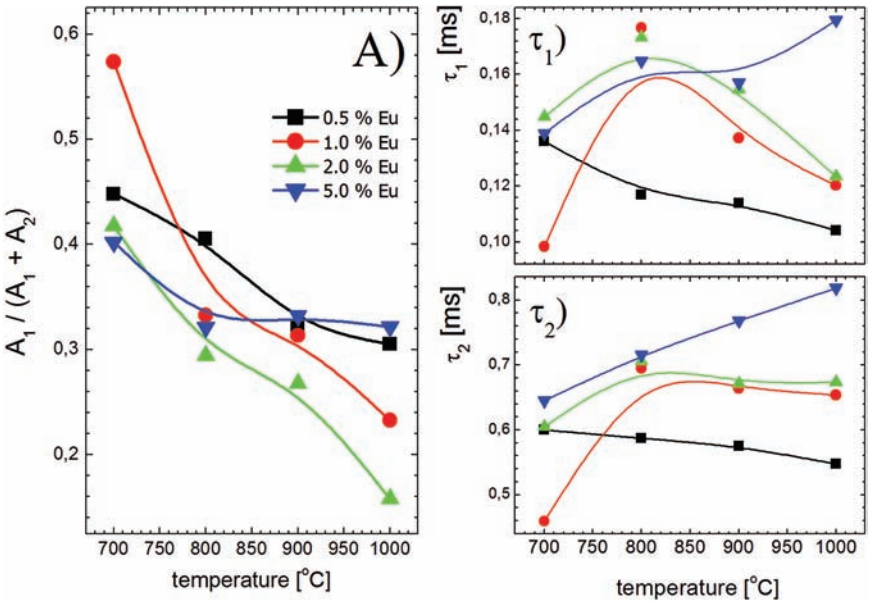

Figure 9. Luminescence lifetime of the $^5D_0$ level analyzed with a double-exponential model. τ_1 and τ_2 indicate short and long decay components, whereas $A_1/(A_1 + A_2)$ indicates the relative intensity of the short component.

is decreased. This, in turn, together with thermally removed impurities (H_2O, postsynthesis remainings) should lead to higher emission quantum yields, and indeed this can be observed in Figure 9. As can be noticed, the contribution of the short decay component decreases for rising sintering temperature. The short component originates from superficial (close to grain boundaries) Eu^{3+} ions; thus, the grain growth leads to a decrease of the grain surface to volume ratio and vanishing surface effects. Astonishingly, the short and long decay values rise with the sintering temperature only for 5.0% Eu-doped samples, whereas they basically decrease for 0.5, 1, and 2% od Eu^{3+}-doped samples. One could expect the opposite behavior; however, crystallographic distortions varied with Eu^{3+} doping and the sintering temperature. The luminescence lifetimes for the 700 °C annealed sample may be regarded as anomalous. An increase of covalent bonding is responsible for a larger transition probability of the $^5D_0 \rightarrow {}^7F_2$ hypersensitive transition.

Both the position and line width of the nondegenerate $^5D_0 \rightarrow {}^7F_0$ transition are direct measures of the local bonding environment and coordination of the Eu^{3+} ion.[31] The peak position of the $^5D_0 \rightarrow {}^7F_0$ transition is related to the nephelauxetic effect, which shifts the center of gravity of the J states. The shift to higher energy in the band maximum indicates that the chemical bond between Eu^{3+} and ligands becomes more covalent. Factors like the local crystal field, electron−phonon coupling, and ion−ion interaction contribute to the broadening of $^5D_0 \rightarrow {}^7F_J$ (J = 1−4).

To gain some insight into the nature of the luminescence behavior of Eu^{3+} ions in nanocrystalline YVO_4 powders, the Judd−Ofelt model was applied for the determination of spontaneous emission coefficients. The intensity parameters Ω_2 and Ω_4 were determined from luminescence spectra following the method originally described by Kodaira et al.[32] Calculations have been performed according to the procedure described in another article.[33] The values of the Ω_2 and Ω_4 parameters as well as other quantities derived from analysis of the luminescence spectra of Eu^{3+}-doped YVO_4 nanocrystals are listed in Table 2.

One may note that the calculated values of the Ω_2 and Ω_4 parameters respond in a similar way to changes in the annealing

Table 2. Decay Rates of Radiative (A_{rad}) and Nonradiative (A_{nrad}) Processes of $^5D_0 \rightarrow {}^7F_J$ Transitions, Luminescence Lifetimes (τ), Intensity Parameters (Ω_2 and Ω_4), and Quantum Efficiencies (η) Determined from Photoluminescence Spectra

concn [%]	annealing temp [°C]	A_{rad} [s^{-1}]	A_{nrad} [s^{-1}]	τ [ms]	Ω_2 [10^{-20} cm^2]	Ω_4 [10^{-20} cm^2]	η [%]
0.5	700	1022	1475	0.40	5.08	1.50	40.9
	800	797	1604	0.42	3.87	1.24	33.2
	900	812	1403	0.45	3.92	1.30	36.6
	1000	785	1494	0.44	3.84	1.14	34.5
1	700	944	2993	0.25	4.64	1.45	24.0
	800	898	991	0.53	4.41	1.36	47.5
	900	748	1178	0.52	3.66	1.05	38.8
	1000	788	1009	0.56	3.83	1.19	43.8
2	700	934	1441	0.42	3.83	1.40	39.3
	800	918	875	0.56	4.53	1.35	51.2
	900	753	1074	0.55	3.66	1.12	41.2
	1000	803	839	0.61	3.95	1.14	48.9
5	700	890	1310	0.45	4.37	1.34	40.4
	800	890	927	0.55	4.33	1.41	49.0
	900	927	795	0.58	4.56	1.41	53.8
	1000	810	800	0.62	3.90	1.32	50.3

temperature of the samples as well as in the Eu^{3+} concentration. Many studies have shown that the Ω_2 parameter is sensitive to both asymmetry and covalency at the RE^{3+} site.[34] Basically, the Ω_2 in our samples decrease with an increase of the annealing time. For the 700 °C sample, Ω_2 and Ω_4 tend to monotonically decrease with the Eu^{3+} concentration. For higher Eu^{3+} concentrations, the behavior of Ω_2 and Ω_4 is mixed versus the Eu^{3+} doping level but generally both parameters decrease versus the annealing time. The first dependence (i.e., Ω_2 vs $[Eu^{3+}]$) may be related to increasing covalency of $Eu^{3+}-O^{2-}$ bond (also visible in the excitation spectra as a shift of the CT maximum), while the second one (i.e., Ω_2 vs T [°C]) may result from a decrease of the asymmetry of the Eu^{3+} site. Better crystallization

dx.doi.org/10.1021/ic202444s | Inorg. Chem. 2012, 51, 1180−1186

and growth of the nanocrystals at higher annealing temperature obviously result in ordering of the structure. The value of the Ω_4 intensity parameter is not directly related to the symmetry of the Eu^{3+} ions but, mostly, to the electron density on the surrounding O^{2-} anions.[35] Therefore, calculated values are weakly dependent on the annealing temperature, which caused structural changes, but are gained by increasing Eu^{3+} concentration. As mentioned above, Eu^{3+} cations decrease the ionicity of the $Eu^{3+}-O^{2-}$ band.

Luminescence Decays. Luminescence lifetimes were non single exponents, and good fits required a double-exponential model to be used. As one may see in Figure 9, the short component's contribution to the observed luminescence decay is decreases for all of the studied Eu^{3+} concentrations versus the annealing time. The observed change is significant because it drops from ~40−60% for the smallest nanoparticles down to 15−30% for the highest sintering temperatures. This may indicate the removal of water molecule residuals on the surface of the nanocrystal, which is known to quench Eu^{3+} luminescence. With an increase of annealing, the short decays (τ_1) do not change much in the opposite to long decay component (τ_2). The two decays may be linked to the emission from two Eu^{3+} sites, although emission spectra (as in Figure 7) do not demonstrate evidence of the presence of two sites. Probably, during the formation of the nanocrystals, Eu^{3+} ions locate on the nanocrystal surface. This induces interactions with the surrounding environment and quenches the excited state of the Eu^{3+} ions. An increasing concentration of the dopant forces allocation of Eu^{3+} ions in sites inside the nanocrystals and, consequently, the lifetimes are lengthened. The presence of two decay components may also result from the large surface to volume ratios (S/V) found in nanomaterials. While the 0.5% Eu^{3+} sample demonstrates a slight monotonic decrease of τ_2, τ_2 significantly rises for the 5% Eu^{3+}-doped sample. The former result is difficult to explain; the latter results most probably from decreasing S/V ratio.

■ CONCLUSIONS

In the present work, YVO_4 nanopowders were prepared by the sol−gel method. The structural and spectral properties were studied for the samples containing different amounts of Eu^{3+}. Moreover, XRD and TEM analysis demonstrated a significant dependence of the nanoparticle size and structure on the calcination temperature, which was varied between 700 and 1000 °C. We have found that the size effect manifests mainly in the expansion of the cell volume and broadening of the XRD peaks as indicated by Rietveld analysis. Additionally, the emission and excitation spectra, although typical for Eu^{3+} ions, demonstrated some degree of variability with these two parameters. By employment of the Judd−Ofelt theory, we could confirm that the Eu^{3+}-doped YVO_4 nanomaterial luminescence is predictibly susceptible to the local crystallographic and chemical environment.

■ AUTHOR INFORMATION

Corresponding Author

*E-mail: R.Wiglusz@int.pan.wroc.pl. Phone: +48-71-3954-159(166). Fax: +48-71-344-10-29.

■ REFERENCES

(1) Fields, R. A.; Birnbaum, M.; Fincher, C. L. *Appl. Phys. Lett.* **1987**, *51*, 1885−1886.
(2) Oconnor, J. R. *Appl. Phys. Lett.* **1966**, *9*, 407.
(3) Gerner, P.; Kramer, K.; Gudel, H. U. *J. Lumin.* **2003**, *102*, 112−118.
(4) Palilla, F. C.; Levine, A. K.; Rinkevic, M. *J. Electrochem. Soc.* **1965**, *112*, 776.
(5) Rambabu, U.; Amalnerkar, D. P.; Kale, B. B.; Buddhudu, S. *Mater. Res. Bull.* **2000**, *35*, 929−936.
(6) Hou, Z. Y.; Yang, P. P.; Li, C. X.; Wang, L. L.; Lian, H. Z.; Quan, Z. W.; Lin, J. *Chem. Mater.* **2008**, *20*, 6686−6696.
(7) Yu, M.; Lin, J.; Wang, Z.; Fu, J.; Wang, S.; Zhang, H. J.; Han, Y. C. *Chem. Mater.* **2002**, *14*, 2224−2231.
(8) Ekambaram, S.; Patil, K. C. *J. Alloys Compd.* **1995**, *217*, 104−107.
(9) Fey, G. T. K.; Huang, D. L. *Electrochim. Acta* **1999**, *45*, 295−314.
(10) Haase, M.; Riwotzki, K.; Meyssamy, H.; Kornowski, A. *J. Alloys Compd.* **2000**, *303*, 191−197.
(11) Huignard, A.; Gacoin, T.; Boilot, J. P. *Chem. Mater.* **2000**, *12*, 1090−1094.
(12) Riwotzki, K.; Haase, M. *J. Phys. Chem. B* **1998**, *102*, 10129−10135.
(13) Yoshimura, M.; Byrappa, K. *J. Mater. Sci.* **2008**, *43*, 2085−2103.
(14) Wu, H.; Xu, H. F.; Su, Q.; Chen, T. H.; Wu, M. M. *J. Mater. Chem.* **2003**, *13*, 1223−1228.
(15) Wang, Y. H.; Zuo, Y. Y.; Gao, H. *Mater. Res. Bull.* **2006**, *41*, 2147−2153.
(16) Wu, X. C.; Tao, Y. R.; Mao, C. J.; Liu, D. J.; Mao, Y. Q. *J. Cryst. Growth* **2006**, *290*, 207−212.
(17) Wu, X. C.; Tao, Y. R.; Song, C. Y.; Mao, C. J.; Dong, L.; Zhu, J. J. *J. Phys. Chem. B* **2006**, *110*, 15791−15796.
(18) Wang, J.; Xu, Y. H.; Hojamberdiev, M.; Peng, J. H.; Zhu, G. Q. *Mater. Sci. Eng. B: Adv.* **2009**, *156*, 42−47.
(19) Scherrer, P. *Nachr. Ges. Wiss. Göttingen* **1918**, 98−100.
(20) Chakoumakos, B. C.; Abraham, M. M.; Boatner, L. A. *J. Solid State Chem.* **1994**, *109*, 197−202.
(21) Rietveld, H. M. *J. Appl. Crystallogr.* **1969**, *2*, 65.
(22) Delhez, J. L.; de Keijser, T. H.; Langford, J. I.; Louër, D.; Mittemeijer, E. J.; Sonneveld, E. J. *Crystal Imperfection Broadening and Peak Shape in the Rietveld Method*; Oxford University Press: Oxford, U.K., 1993; *Vol. 132*.
(23) Lutterotti, L.; Matthies, S.; Wenk, H. R. *IUCr Newsletter CPD* **1999**, *21*, 14−15.
(24) Ayyub, P.; Palkar, V. R.; Chattopadhyay, S.; Multani, M. *Phys. Rev. B* **1995**, *51*, 6135−6138.
(25) Palkar, V. R.; Ayyub, P.; Chattopadhyay, S.; Multani, M. *Phys. Rev. B* **1996**, *53*, 2167−2170.
(26) Wang, Y. H.; Guo, X.; Endo, T.; Murakami, Y.; Ushirozawa, M. *J. Solid State Chem.* **2004**, *177*, 2242−2248.
(27) Xie, L. P.; Song, H. W.; Wang, Y.; Xu, W.; Bai, X.; Dong, B. *J. Phys. Chem. C* **2010**, *114*, 9975−9980.
(28) Huignard, A.; Buissette, V.; Franville, A.-C.; Gacoin, T.; Boilot, J.-P. *J. Phys. Chem. B* **2003**, *107*, 6754−6759.
(29) Kaminskiĭ, A. A. *Crystalline lasers: physical processes and operating schemes*; CRC Press: Boca Raton, FL, 1996.
(30) Georgescu, S.; Cotoi, E.; Voiculescu, A. M.; Toma, O. *Rom. Rep. Phys.* **2008**, *60*, 947−955.
(31) Brecher, C.; Riseberg, L. A. *Phys. Rev. B* **1976**, *13*, 81−93.
(32) Kodaira, C. A.; Brito, H. F.; Malta, O. L.; Serra, O. A. *J. Lumin.* **2003**, *101*, 11−21.
(33) Wiglusz, R. J.; Bednarkiewicz, A.; Lukowiak, A.; Strek, W. *Spectrosc. Lett.* **2010**, *43*, 333−342.
(34) Ebendorff-Heidepriem, H.; Ehrt, D.; Bettinelli, M.; Speghini, A. *J. Non-Cryst. Solids* **1998**, *240*, 66−78.
(35) Nageno, Y.; Takebe, H.; Morinaga, K. *J. Am. Ceram. Soc.* **1993**, *76*, 3081−3086.